Hydrol. Earth Syst. Sci. Discuss., 9, 4465–4503, 2012
www.hydrol-earth-syst-sci-discuss.net/9/4465/2012/
doi:10.5194/hessd-9-4465-2012
© Author(s) 2012. CC Attribution 3.0 License.

Hydrology and Earth System Sciences Discussions

This discussion paper is/has been under review for the journal Hydrology and Earth System Sciences (HESS). Please refer to the corresponding final paper in HESS if available.

Fluorescent particle tracers for surface flow measurements: a proof of concept in a semi-natural hillslope

F. Tauro[1,2,3], S. Grimaldi[1,3,4], A. Petroselli[5], M. C. Rulli[6], and M. Porfiri[1]

[1]Department of Mechanical and Aerospace Engineering, Polytechnic Institute of New York University, Brooklyn, NY 11201, USA
[2]Dipartimento di Ingegneria Civile, Edile e Ambientale, Sapienza Università di Roma, 00184 Rome, Italy
[3]Honors Center of Italian Universities, Sapienza University of Rome, 00184 Rome, Italy
[4]Dipartimento per l'Innovazione nei Sistemi Biologici, Agroalimentari e Forestali, Università della Tuscia, 01100 Viterbo, Italy
[5]Dipartimento di Scienze e Tecnologie per l'Agricoltura, le Foreste, la Natura e l'Energia, Università della Tuscia, 01100 Viterbo, Italy
[6]Dipartimento di Ingegneria Idraulica, Ambientale, Infrastrutture Viarie, Rilevamento, Politecnico di Milano, 20133 Milan, Italy

Received: 17 March 2012 – Accepted: 24 March 2012 – Published: 3 April 2012

Correspondence to: S. Grimaldi (salvatore.grimaldi@unitus.it)

Published by Copernicus Publications on behalf of the European Geosciences Union.

Abstract

In this paper, a proof of concept experiment is conducted to assess the feasibility of tracing overland flow on a semi-natural hillslope plot via a novel fluorescent particle tracer. Runoff on the experimental plot is artificially simulated by using a custom-built rainfall system. Experiments are performed by using beads of diameters ranging from 75 to 1180 µm that are sensed through an experimental apparatus comprising a light source and a video acquisition unit. Particles' transit is detected through an unsupervised methodology based on image analysis techniques and compared to results from supervised visual inspection. Average flow velocity estimations are obtained from travel time measurements of the particles as they are dragged by the overland flow on the hillslope. Velocities are compared to flow measurements obtained using rhodamine dye. Experimental findings demonstrate the potential of the methodology for understanding overland flow dynamics in complex natural settings. In addition, considerations for optimizing the particle size are presented based on the visibility of the beads and their accuracy in flow tracing.

1 Introduction

Hillslope overland flow controls multiple phenomena in natural watersheds, including surface runoff contributing to the basin hydrologic response (Scherrer et al., 2007; Gomi et al., 2008a; McGuire and McDonnell, 2010; Uchida and Asano, 2010); rill development and erosion mechanics influencing soil roughness (Berger et al., 2010; Ghahramani et al., 2011; Mügler et al., 2011); and pollutant diffusion and nutrient loss affecting agriculture and soil management (Ticehurst et al., 2007). Despite their relevant impact on environmental engineering practice, hillslope models are mostly calibrated by using data obtained in controlled laboratory environments. Such data are typically not able to replicate the complexity of phenomena occurring at multiple temporal and spatial scales in real hillslopes. These important models include

HESSD
9, 4465–4503, 2012

sheet-flow formulations (Bronstert and Plate, 1997; Clark et al., 2009), hillslope threshold schemes for rainfall-runoff response (Doody et al., 2010), and empirical overland flow velocity formulas (Mügler et al., 2011).

Major challenges in the implementation of flow measurement systems in hillslopes are due to the ephemeral nature of microchannels along with shallow water depths and high turbidity, the presence of small scale vegetation, and the often poor geographical accessibility (Hudson, 2004). In such adverse conditions, tracing techniques are valid alternatives to commonly used stream flow measurement systems such as electromagnetic and acoustic sensors (Lee et al., 2002; Puleo et al., 2012). In particular, experiments on natural or semi-natural hillslopes often resort to using tracers such as chemicals, naturally occurring water isotopes, dyes, and salts (Dunkerley, 2001; Lange et al., 2003; Planchon et al., 2005; Berman et al., 2009; Speed et al., 2010). Tracer adsorption issues and losses are often minimized by conducting experiments on small scale plots (Tatard et al., 2008; Mügler et al., 2011). Despite their considerable advantages, most tracing technologies require either the tracer detection through bulky sensing probes or laboratory analysis on collected soil and water samples (Tatard et al., 2008; Gomi et al., 2008b). Another monitoring technique frequently used in field studies consists of excavating trenches in the hill and installing troughs and V-notch weirs to intercept and measure overland runoff (Gomi et al., 2008b). Yet, these procedures are highly dependent on the depth of the micro channels (Tatard et al., 2008), are seldom adequate in real-time estimations, and are usually invasive for the environment.

Recently, optical methods have been proposed for the observation of hydrologic phenomena such as flow measurements in shallow channels (Dunkerley, 2003), river bank evolution and erosion patterns (Hauet et al., 2009), and riverine surface current monitoring (Fujita et al., 2007; Dramais et al., 2011; Fujita and Kunita, 2011; Puleo et al., 2012). The implementation of imaging techniques in natural environments is expected to be less invasive than traditional measurement systems and has the potential of being easily automated (Muste et al., 2008). Nonetheless, such approaches typically rely on ambient illumination and presence of foam patterns on the water surface (Muste et al.,

HESSD
9, 4465–4503, 2012

2011; Jodeau et al., 2008). These requirements pose severe challenges in the analysis of small scale highly turbulent flows in vegetated channel beds which are typical of uplands environments. In addition, images can be affected by distortions, thus requiring time-consuming preliminary orthorectification procedures (LeCoz et al., 2010).

In this paper, practical limitations of traditional techniques for monitoring overland flows are mitigated by using a novel tracing methodology based on the deployment and observation of fluorescent particles in natural rills. Specifically, this low-cost measurement system is applied to flow measurements in natural micro channels. Tracer dispersion due to adhesion to naturally present substrates in overland flows is limited by the use of insoluble beads that minimize the amount of tracing material for experiments. Further, the enhanced visibility of the fluorescent particles allows for non-intrusively detecting the tracer through imaging techniques without deploying bulky probes and samplers in the water.

The feasibility of using buoyant fluorescent particles in static and dynamic water conditions in both daylight and dark is demonstrated in Tauro et al. (2010, 2011b). Specifically, in Tauro et al. (2010), turbid suspensions of off-the-shelf buoyant beads of up to 60 $g\,l^{-1}$ are considered to replicate sediment load conditions occurring during heavy floods in mountainous streams. In Tauro et al. (2011b), an automatic image-based analysis procedure is developed to detect and track the particles as they float in the presence of daylight reflections and in turbulent flows, yet, in laboratory conditions. Particle accuracy in tracing different flow velocities is demonstrated through a parametric analysis conducted by using the Basset-Boussinesq-Oseen (BBO) equation (Soo, 1967; Maxey and Riley, 1983). In addition, a proof of concept experiment of the potential of the fluorescent particle tracer methodology as an efficient flow measurement system for outdoor environments is performed in the Rio Cordon stream in the Italian Alps (Tauro et al., 2011a). The particles are therein used to conduct flow measurements at a stream cross-section and travel time experiments in stream reaches of up to 30 m.

HESSD
9, 4465–4503, 2012

In this paper, this tracing methodology is used for a proof of concept experiment in a semi-natural hill. Specifically, travel time measurements are conducted on an experimental hillslope plot equipped with a rainfall simulator and a particle detection system. The detection system, placed across a natural rill at the outlet of the plot, hosts a light source for exciting the beads' fluorescence and a waterproof digital camera for video acquisition. Videos depicting the bead transits are processed through both supervised and unsupervised techniques to obtain average surface velocities of water flowing in the rill. Experiments are conducted by using particles of varying diameters ranging from 75 to 1180 µm. This proof of concept study demonstrates the feasibility of using enhanced visibility micro spheres for monitoring complex environmental flows and providing estimates of surface overland flow velocities. In addition, the equipment used in this study has the potential to be transported on natural hills to estimate flow velocities in ungauged areas.

The rest of the paper is organized as follows. In Sect. 2, the following elements are technically elucidated: the particle tracer and the in house-built experimental detection system; the experimental site including the plot preparation; the image-based analysis procedures used for data processing; and the rainfall simulator. In Sect. 2, a detailed description of the fluorescent particle experiments is also presented. In Sect. 3, experimental results are illustrated and discussed. Conclusions and remarks are presented in Sect. 4. The calibration of the rainfall system is reported in Appendix A.

2 Materials and methods

2.1 Fluorescent particle tracer apparatus

The buoyant fluorescent particles used in this study are purchased from Cospheric LLC (http://www.cospheric-microspheres.com). The spheres are white under daylight and emit yellow-green light (561 nm wavelength) if excited by a UV light source (365 nm wavelength), see Fig. 1. The particles are made of polyethylene and their fluorophore

HESSD
9, 4465–4503, 2012

is embedded in the polymer matrix which allows for a long luminescence lifetime and enhanced and uniform visibility. The spheres are slightly buoyant and their nominal dry density is 0.98 g cm^{-3}. Table 1 indicates the classes of particles used in this proof of concept experiment ordered in terms of their diameter. This wide spectrum of diameters is used to establish guidelines for particle selection in tracing shallow waters in natural conditions.

Particles' transits are recorded as the beads float on the rill water surface underneath the experimental detection apparatus first introduced in Tauro et al. (2011a). The apparatus hosts both light source and video acquisition units, see Fig. 2. A telescopic system of vertical aluminum bars is connected to the lamp case and allows for regulating image illumination by adjusting the distance of the light source from the water surface. The case contains an array of 14 UV 8 W lamps in parallel and series connections. A low cost water proof Bullet HD 1080p camera is located on a tripod head connected to a vertical aluminum bar. The Bullet camera is manually operated and set at 1920 × 1080 pixels resolution for video recording at the acquisition frequency of 30 Hz. A compensating counterbalance is used to adjust the distance of the camera from the surface of interest. A metric ruler installed on aluminum rods allows for calibration of the acquired videos. The distance of the video acquisition unit from the surface and light source can be adjusted according to illumination and dimensions of the field of view. In dim illumination conditions, a 568 nm optical filter is placed on the Bullet camera to emphasize particle brightness.

2.2 Experimental site

Experiments are performed in a terrain parcel in the Azienda Agraria at the University of Tuscia, Viterbo, Italy, where a semi-natural 40 m^3 hillslope is prepared, see Fig. 3. The plot is 1.7 m high, 6.5 m long, and 3 m wide and it is covered by grass only for the 10 %. The granulometry of the soil is provided in Table 2. In the center of the plot, a mild concavity is preliminary raked to create a preferential path to rainfall and then irrigated for a few hours. After irrigation, a 4 m long central rill is formed in the plot and

HESSD
9, 4465–4503, 2012

the experimental detection apparatus is located at its terminal part, see Fig. 3. The slope of the hill is approximately equal to 17° and shows a slight concavity after a few rainfall experiments. A rainfall simulator is placed on the top corner of the plot, see Fig. 3, to provide a uniform rain distribution on the entire hill. The particle deployment section is marked with wooden strikes at approximately 4 m upstream of the detection setup. Four additional wooden strikes are installed one meter apart along the rill from the upstream section.

2.3 Particle detection procedure

Travel time experiments are conducted by synchronizing particle deployment and video acquisition. Particle travel time is identified as the time the beads take to flow from the deployment section on the plot to the detection apparatus along the 4 m long rill. The arrival of the particles at the detection setup refers to when the particles enter the field of view of the camera. The transit of the particles is identified through image-based analysis tools by converting captured videos into RGB frames and then analyzing the sole green channel where particle emissions are more evident. In particular, gray-scale frames are processed by using a modified version of the following index $\mathcal{G}$ defined by (Tauro et al., 2010),

$$\mathcal{G} = \frac{\sum_{i \in \mathcal{J}} (c_i)^{\alpha} \, n_i}{\sum_{i \in \mathcal{J}} n_i}, \; \mathcal{J} = \{i \in \{0, 1, \ldots, 255\} : n_i > 0\}, \tag{1}$$

with $n_i = n_i^p - n_i^b$. Here, n_i^b and n_i^p refer to the pixel count for the background and particle images, respectively. The term c_i represents the pixel intensity classes from 0 to 255 where the power α is introduced to assign a higher weight to the exiguous number of bright pixels in the entire image corresponding to the particles. In particular, the exponent α is set to 10 throughout the whole set of experiments to emphasize brighter pixels against the background. The relatively high value of the exponent is

HESSD
9, 4465–4503, 2012

motivated by the particularly adverse illumination and environmental conditions and is found by performing a preliminary analysis on a single video where the value of the exponent is varied until eventual peaks in the index are clearly identified. It is noted that background images are obtained from the original ones by applying a bottom-hat transformation (Haralick et al., 1987; Gonzalez et al., 2004). Peaks in the index $\mathcal{G}$ correspond to sequences of frames where brightness is maximized and therefore where the particles are more likely to be (Tauro et al., 2010).

Experiments performed in outdoor environments are particularly challenging due to the presence of external and uncontrolled light sources, water surface reflections, and extraneous objects and sediments that affect the quality of captured images and increase uncertainty in the index computation. Therefore, signal noise is partially filtered by introducing an automatic procedure to identify the beads. Specifically, a moving average of the time trace of the index is computed for each experimental video by using subsets of ten consecutive images. For convenience, such filtered time trace is referred to as G. Then, particles' transits in the signal are automatically detected by locally fitting G with a gaussian function, while constantly skipping 15 values of G to reduce computational cost. The nonlinear least square method is used to perform the fitting and its goodness is ascertained by imposing that the coefficient of determination is equal or greater than 0.85.

The sequence of frames identifying the transit of the particles is found by imposing further constraints on the fitting window which presents the highest coefficient of determination. In particular, the mean value of the fitting gaussian function is required to lay in the interval $[m - 0.15\ l,\ m + 0.15\ l]$, where m is the mean time in the window of interest and l corresponds to the length of the window. In addition, constraints are imposed on the minimum and maximum values of G in the analyzed window. Specifically, the presence of a peak in the intensity is assessed by imposing $0.4 \leq (\max G - \min G)/\max(G) \leq 1$ in the fitting interval. Experimental videos satisfying such constraints lead to the identification of particles' transit. As the brightest frame sequences are determined, the frame order number corresponding to the first value

HESSD
9, 4465–4503, 2012

of G in the fitting window is divided by the camera acquisition frequency and used to calculate the beads travel time. This identification procedure is repeated using different windows of three different lengths of 50, 100, and 150 values of G to accommodate for varying duration of particles' transit. If multiple successful readings are obtained for these different lengths, corresponding values are averaged.

2.4 Rainfall simulator

The plot rainfall system consists of a pressurized nozzle rainfall simulator (Esteves et al., 2000; Pérez-Latorre et al., 2010). The simulator is designed and developed based on the prototype by Riley and Hancock (1997). The basic structure of the simulator comprises a telescopic aluminum tripod connected to a steel plate. Three hoses are riveted to the plate and water is sprayed through a system of three nozzles as displayed in Fig. 4. Specifically, an HH7-M 3/4 in nozzle is mounted on the central hose whereas two smaller HH22-M 3/8 in nozzles are placed onto the lateral hoses. Three cut-off valves allow for selectively activating the nozzles and controlling rainfall intensity. Water is supplied to the hoses through a plastic reinforced tube connected to the steel plate through a sleeve coupling. Rainfall intensity is regulated by using a pressure gauge. Water is jetted from an height of approximately 2.7 m from the ground and can cover an area of approximately $7 \times 7\,m^2$. Rainfall intensities can be varied from a minimum of $40\,mm\,h^{-1}$ by using the two smaller nozzles to $140\,mm\,h^{-1}$ by operating the three nozzles simultaneously. The calibration of the rainfall simulator uniformity and intensity is presented in Appendix A.

2.5 Experiment description

Travel time experiments are conducted by activating the rainfall simulator at the constant intensity of approximately $50\,mm\,h^{-1}$ to produce a water depth of a few centimeters in the rill. The particle detection apparatus is placed at the flat base of the hillslope, that is, at the terminal section of the rill with the Bullet camera and the lamp

HESSD
9, 4465–4503, 2012

unit at approximately 20 cm from the rill bed. To prevent excessive distortions in videos, the camera is angled at 70° from the horizontal. The simulator nozzles are placed at an height of approximately 2.3 m from the soil on the top of the hillslope.

For each experiment, a sample of 4–5 g of particles of a selected diameter class is deployed at the rill onset at approximately 4 m from the detection apparatus. The instant of deployment and the beginning of the video are synchronized with a precision of approximately 0.1 s. Such precision is achieved by using a chronometer synchronized with the camera. For each class of particle diameters, ten repetitions are performed. The rainfall simulator is active for the entire duration of the experiments. Once videos are taken, frames are processed to estimate travel time. Surface flow velocity is then computed by dividing the total length of the rill by the particle travel time.

Before and after each experiment, the width and depth of the rill at the strikes sections and underneath the detection apparatus are measured to account for erosion and sediment transport phenomena and to monitor rill bed evolution. In addition, experiments are performed over one month and during sunny days in absence of strong wind to limit possible biases in the uniformity of the simulated rainfall. To prevent destructive rill bed erosion and sediment wash-off, the plot is covered with a waterproof cloth during rainy days.

3 Results and discussion

3.1 Supervised analysis

Ten videos for each class of bead diameters are converted to frames and manually analyzed to observe the transit of the particles. This supervised visual analysis demonstrates the enhanced detectability of the fluorescent particles in complex conditions. Specifically, particles from all classes are generally visible in the area captured by the camera despite poor image quality. Image quality is influenced by a number of factors.

HESSD
9, 4465–4503, 2012

It is noted that experiments are performed in extremely adverse illumination conditions, that is, under direct sunlight in the early afternoon. The effect of reflections and excessive illumination is partially mitigated by creating a shadowy zone on the detection apparatus through black panels. Nonetheless, light can sensibly affect image quality and visibility of the fluorescent particles. Challenges in detecting the particles are also due to the meagre quantity of tracer deployed for each experiment, that is, only 4–5 g. Further, an array of concurring parameters tends to dismember the group of beads once deployed in the rill. Specifically, rain drops falling onto the water surface create small waves and vortices that contribute to disperse the cloud of beads. The complex structure and morphology of the rill bed and the presence of severe sediment loads are other causes of particle dispersal. After an initial phase when runoff mainly occurs in the form of sheet-flow on the soil surface, the onset of rilling develops through a super-critical flow velocity regime (Tatard et al., 2008). This condition produces the formation of small hydraulic jumps and pools where sediments are massively transported from higher-gradient regions, that is, the top of the hillslope plot, to downstream tracts. The rill evolves towards a small scale step-and-pool microchannel where velocity alternates from placid zones to faster reaches. In such settings, samples floating in the rill tend to remain trapped in pool sections. Isolated beads are then gradually released from the pools. This phenomenon tends to affect mostly the visibility of particles of smaller diameters which are harder to see in small quantities.

Three different behaviors can be observed by visually analyzing recorded videos according to the specific dimensions of the particle tracer. For particles of diameters ranging from 75 to 180 µm, deployed samples appear as a white powder as they flow along the rill, see Fig. 5. Therein, a channel reach where beads tend to be trapped at the outside bend of the rill into small vortical structures is shown. Particles are then released in small clouds downstream of the bend that are hardly visible when reaching the detection section. On the other hand, when larger clouds of particles gather in the camera field of view, their identification is possible. Figure 6 displays the transit of a cloud of 75–90 µm beads as captured by the camera. The powder crosses the region

HESSD
9, 4465–4503, 2012

of interest, that extends for approximately 8 cm, in 18 frames. Note that snapshots in Fig. 6 are not orthorectified. Therein, the particle cloud compactly travels throughout the entire length of the region of interest making the beads easily detectable by the operator. In addition, fluorescence is clearly recognizable against the background even though water turbidity and suspended sediment load are remarkable.

Conversely, particles ranging from 710 to 1180 µm do not flow in clusters along the rill but tend to disperse as they are deployed. In Fig. 7, a sample of particles of larger diameters flowing in the rill is shown. The picture captures the dispersion of the bead cloud due to the presence of sediments and subrills. Samples travel in the form of particle trains, that is, isolated particles that are still visible at the detection section due to their relatively large size. In particular, Fig. 8 displays the transit of isolated particles of 1000–1180 µm in diameter. In this case, the particle train is highly elongated and its entire passage is difficult to identify. Specifically, the transit of the sample is detected as a sequence of independent particles in the camera field of view.

Particles of intermediate sizes, that is, beads ranging from 250 to 600 µm, are affected by a combination of the two formerly described behaviors. In particular, dispersal of the sample tends to occur from the very deployment into the rill similarly to particle of diameters in the range 710–1180 µm. Differently from the latter particles, beads ranging from 250 to 600 µm are not distinctly visible when reaching the detection apparatus due to their rather small dimensions. These factors critically affect the detection of the particles by visual inspection.

Travel times computed through visual inspection are obtained by identifying the frame where beads first appear in the camera's region. Since the camera acquisition and particle deployment are synchronized, the time taken by the particle to reach the detection apparatus is easily found by dividing the frame order number by the camera acquisition frequency. Velocity is then obtained by dividing the travel time by the approximate length of the rill, that is, 4 m.

Two additional travel time experiments are performed by deploying rhodamine WT dye in the rill to compare findings from the fluorescent particle tracer to a more common

HESSD
9, 4465–4503, 2012

methodology. Experiments with rhodamine are conducted by releasing 0.5 ml of dye at the deployment section and by synchronizing the release with the acquisition of the digital camera. The time the dye takes to flow along the 4 m long rill is found by converting experimental videos into frames and then manually analyzing images. The first frame at which the presence of the dye is observed is then divided by the acquisition frequency of the digital camera to recover the travel time.

Estimations of the travel time through visual inspection are generally possible for videos depicting transits of the 1000–1180 µm particles. In this case, the analysis gives an average velocity of 0.33 m s^{-1} over the ten experimental repetitions with a standard deviation of 0.02 m s^{-1}. This value is in good agreement with velocity obtained by using the rhodamine dye, that is, 0.34 m s^{-1} with standard deviation 0.01 m s^{-1}. Experiments with smaller particles do not lead to accurate estimations of travel time due to the poor visibility of first beads arrival and potential dispersion.

3.2 Unsupervised analysis

The above discussion on particle visibility is confirmed by the unsupervised analysis of the experimental videos. Specifically, Fig. 9 displays the time trace of the index $\mathcal{G}$ for three representative experiments for particles of diameters equal to 75–90 µm, 1000–1180 µm, and 500–600 µm, respectively. The peak at frame 1366 in Fig. 9a pertains to the passage of the cloud of particles depicted in Fig. 6. Two peaks and higher values of the index are observed from frame 694 to 791 in Fig. 9b, relative to the snapshots shown in Fig. 8. On the other hand, in Fig. 9c, no peak is clearly evident. Such findings confirm that the index successfully detects the transit of bright clusters of particles even if it likely fails to identify the arrival of the first beads of small diameters. It is also observed that intensities in Fig. 9b are lower than intensities of the peak in Fig. 9a. Therefore, higher index values in Fig. 9b are more likely to pertain to isolated particles flowing through the region of interest as anticipated from the supervised analysis. Finally, particles of intermediate sizes are not detected by the index.

HESSD
9, 4465–4503, 2012

Further, it is noted that sequences of images identifying the transit of smaller beads do not always produce appreciable peaks in the index. This is attributed to the limited fluorescence intensity of small clusters of beads in the rill. On the other hand, large clouds of particles of smaller diameter crossing the camera field of view as in Fig. 6 generate peaks in $\mathcal{G}$. In case of the larger diameters, 1000-1180 µm particle trains produce peaks in $\mathcal{G}$ for almost each experiment. Finally, the index fails to detect particle transits for intermediate diameters.

The identification procedure described in Sect. 2.3 is applied to each of the ten experimental repetitions recorded for the studied diameters to automatically obtain particle travel time. The only green channel of the images is analyzed and frames are preliminary cropped to restrict particle search to the portion of the image depicting the rill bed.

Experimental videos respecting the constraints imposed through the fitting procedure are reported in Table 3. Specifically, two videos are fitted for the 75–90 µm, five for the 150–180 µm, one for the 710–850 µm, and three for the 1000–1180 µm diameters. Travel time is estimated from the frame order number corresponding to the first value of G in the fitting window and velocities relative to each fitting are presented in Table 3.

Results in Table 3 show that unfeasible velocities are obtained for the smaller particles and therefore confirm that the index is not able to detect first arrivals for beads of diameters of 150–180 µm and smaller. Nonetheless, the fitting procedure can be used to sense the transit of particle clouds of small dimensions. Notably, four experiments out of the five reported in Table 3 for 150–180 µm diameters pertain to the actual transit of the beads whereas the velocity value equal to 1.47 m s^{-1} is biased by reflections on the water surface. On the other hand, larger particles, such as the 1000–1180 µm spheres, are easier to detect and estimated velocities are comparable to values obtained from visual analysis and experiments with rhodamine. Such finding is also confirmed from analysis of Fig. 9. Indeed, the group of 75–90 µm beads in Fig. 9a) is likely not the first cluster of particles to arrive at the detection apparatus since the peak only occurs 37 s after sample deployment, which corresponds to the unreasonable flow

HESSD
9, 4465–4503, 2012

velocity of 0.11 m s^{-1}. Conversely, Fig. 9b) captures the whole transit of the particles as higher values of the index are measured for approximately 3–4 s. It is further observed that longer fitting windows are required for larger diameters due to the fact that particle samples of larger dimensions tend to diffuse in the rill and, therefore, bead trains take longer time to cross the region captured by the camera.

As evidenced by the supervised and unsupervised analysis, the 1000–1180 µm beads can be identified as the optimal particles to be adopted for the experimental settings of this study. In particular, velocities obtained from the automatic procedure are only 15 % lower than estimates from visual analysis and results from both methodologies are close to velocity estimated with the rhodamine dye. Promising results are also found for four out of ten experiments with the 150–180 µm beads, see Table 3. Specifically, the index is able to capture the passage of groups of particles of such small diameters for half of the experiments.

It is further commented that the use of the index implicitly assumes that particles are the brightest objects in recorded image (Tauro et al., 2010). In this study, frames are highly affected by reflections and critical illumination conditions and, therefore, such hypothesis may not be appropriate. In particular, adverse settings impact the detectability of smaller groups of particles flowing in the rill thus hampering the estimation of first arrivals. Nonetheless, the automatic procedure demonstrates a great potential in such critical experimental conditions. Notably, particles' transits are successfully captured by the index for most of larger diameters and for the 150–180 µm beads. Therefore, improving on the experimental apparatus, increasing the quantity of deployed particles, and exploring alternative fluorophores and materials to further enhance the visibility of the beads may significantly aid bead detection through the identification procedure. In addition, encouraging results achieved with the 150–180 µm particles suggest that this diameter could be successfully used for tracing flows in small rills, provided the visibility of the particles is improved. Such diameters may be particularly useful in tracing overland flow in the presence of vegetation which may trap bigger beads along rills thus biasing the estimation of flow velocity.

HESSD
9, 4465–4503, 2012

4 Conclusions

In this paper, a novel fluorescent particle tracer is used to perform a proof of concept experiment to estimate overland flow velocity on a hillslope plot. A custom-built rainfall simulator is designed and calibrated to reproduce natural runoff on the hill. Particles are detected as they flow in the rill underneath a detection apparatus comprising light source and video acquisition units.

Experimental findings demonstrate the feasibility of using the particles for environmental applications. In particular, the enhanced visibility of the beads allows for detecting diameters as small as 75 µm by mere visual inspection. Further analysis are conducted by using an automatic detection procedure based on basic image analysis tools. The methodology is able to automatically identify the transit of clouds of particles as small as 75 µm.

Moreover, overland flow velocity is estimated from experimental videos using travel time. Whereas velocity estimates cannot be rigorously computed for small diameters, promising results are obtained for the largest sizes, that is, 1000–1180 µm. In particular, velocities estimated for such diameters are in good agreement with measurements taken with rhodamine dye. Velocity values obtained from the unsupervised procedure are also comparable to visual inspection analysis.

Future ameliorations to the illustrated methodology will encompass the design of enhanced biodegradable particle tracers and of the hardware components of the detection apparatus. Specifically, better beads may be fabricated by using more environmentally friendly materials thus allowing the deployment of larger batches and by engineering their fluorescence to emit at narrower wavelength ranges. Further, using advanced fluorescent particles will allow to miniaturize the detection apparatus thus leveraging the versatility of the methodology.

HESSD
9, 4465–4503, 2012

Appendix A

Rainfall simulator calibration

A1 Rainfall uniformity and intensity

Calibration experiments on the rainfall simulator are conducted in an outdoor space where wind effects are minimal. Micro rain gauges are distributed on the nodes of a $7 \times 7\,m^2$ square grid at the reciprocal distance of 1 m and with the simulator positioned at the center of the square, see Fig. A1. The diameter of the rain gauges is equal to 68 mm.

The simulator is tested for the following configurations of the nozzles: the two HH22-M 3/8 in nozzles are activated (C1); one HH22-M 3/8 in and one HH7-M 3/4 in nozzle are opened (C2); and each nozzle is opened and spraying (C3). Experiments are conducted by varying the pressure of the simulator from 0.4 to 1.8 bar. During each experiment, the simulator is activated at a constant pressure for a duration of 15-45 minutes. At the end of the experiment, rain gauges are weighted and rain intensity values are obtained for each node of the square grid. Four repetitions are conducted for each nozzle configuration. Rainfall intensities computed over uniform space grids of $3 \times 3\,m^2$ and $5 \times 5\,m^2$ are displayed in Fig. A2. Despite the simulator spray reaches an area of $7 \times 7\,m^2$, rainfall is highly nonuniform in the external wet belt. Such results are thus omitted. In Fig. A2, maximum levels of rainfall intensity are obtained by letting the three nozzles simultaneously opened.

A characterization of the spatial rainfall variability of the simulator is assessed by computing the coefficient of uniformity (CU). As introduced in Christiansen (1941), CU is defined as

HESSD
9, 4465–4503, 2012

$$CU = 100\left(1 - \left(\frac{\sum_{i=1}^{i=n}\left|X_i - \overline{X}\right|}{\overline{X}}\right)\right) \quad \text{(A1)}$$

where X_i is the rainfall intensity obtained from a single micro rain gauge, $\overline{X}$ is the mean rainfall intensity, and n is the number of available rainfall data. Mean percentage values for CU are reported in Table A1 for each experimental configuration.

As expected, good uniformity is obtained for each configuration in case of smaller plots. Nonetheless, acceptable values are also found for the $5 \times 5\,m^2$ plot for configurations C2 and C3. Lower CU values for configuration C1 are related to the fact that the two HH22-M 3/8 in nozzles unevenly distribute rain on the surface of interest. This effect is compensated for when the HH22-M 3/8 in nozzle is active.

A2 Rainfall characterization with parsivel disdrometer

A characterization of the drop size distribution (DSD) and velocity is performed through calibration experiments with the OTT Parsivel optical disdrometer. Specifically, the rainfall simulator nozzles are placed at approximately 1.5 m above the optical disdrometer and are activated for approximately 15 min. Two repetitions are conducted for each experimental configuration presented in Sect. A1. During the experiment, pressure is varied in the range 0.4–0.6 bar.

After each calibration experiment, the number of hydrometeors for 32 classes of diameters and velocities is obtained. Average values obtained from the two repetitions are plotted in Fig. A3. Here, experimental values are compared to commonly used empirical relations by Gunn and Kinzer (1949), Atlas et al. (1973) and Lhermitte (1971). It is observed that the majority of the drop diameters concentrates around 1 mm. This value is in good agreement with real drop size distribution data as illustrated in Löffler-Mang (2000) and Esteves et al. (2000). On the other hand, velocity of the rainfall

HESSD
9, 4465–4503, 2012

simulator drops tends to be lower than naturally observed data for cases C2 and C3. This can be due to the fact that the simulator nozzles are placed at only 1.5 m above the disdrometer. Higher velocities at small diameters are instead obtained for case C1. These results may be due to the uneven rain distribution of configuration C1, see Sect. A1, and, therefore, suggest that the use of the two HH22-M 3/8 in nozzles is not ideal for simulating natural precipitations. Colorbar in Fig. A3 indicates the percentage number of drops for each class of diameter and velocity. In Fig. A3, the majority of the hydrometeors' diameters and velocities lay in the proximity of empirical values from Gunn and Kinzer (1949), Atlas et al. (1973) and Lhermitte (1971). This posits that simulated rainfall is representative for natural precipitations when configuration C2 and C3 are adopted and, therefore, alleges the feasibility of replicating natural drainage by using the simulator.

Acknowledgements. This work was supported by the MIUR Project PRIN 2009 N. 2009CA4A4A "Studio di un tracciante innovativo per le applicazioni idrologiche", by the National Science Foundation under Grant Nos. CMMI-0745753 and CMMI-0926791, and by the Honors Center of Italian Universities (H2CU Sapienza Università di Roma). The authors would like to greatly thank L. Baldini and E. Gorgucci from the Italian National Research Council and E. Adirosi and S. Sebastianelli from Sapienza University of Rome for their collaboration in conducting the simulator calibration with the Parsivel disdrometer and G. Ubertini for conducting the granulometry analysis. Further, R. Rapiti, G. Cipollari, I. Capocci, G. Mocio, and C. Pagano are acknowledged for the realization of the experimental apparatus and help with the experiments.

References

Atlas, D., Srivastava, R. C., and Sekhon, R. S.: Doppler radar characteristics of precipitation at vertical incidence, Rev. Geophys. Space Phys., 11, 1–35, 1973. 4482, 4483, 4503

Berger, C., Schulze, M., Rieke-Zapp, D., and Schlunegger, F.: Rill development and soil erosion: a laboratory study of slope and rainfall intensity, Earth Surf. Proc. Land., 35, 1456–1467, 2010. 4466

HESSD

9, 4465–4503, 2012

Berman, E. S. F., Gupta, M., Gabrielli, C., Garland, T., and McDonnell, J. J.: High-frequency field-deployable isotope analyzer for hydrological applications, Water Resour. Res., 45, W10201, doi:10.1029/2009WR008265, 2009. 4467

Bronstert, A. and Plate, E. J.: Modelling of runoff generation and soil moisture dynamics for hillslopes and micro-catchments, J. Hydrol., 198, 177–195, 1997. 4467

Christiansen, J. E.: The uniformity of application of water by sprinkler system, Agr. Eng., 22, 89–92, 1941. 4481

Clark, M. P., Rupp, D. E., Woods, R. A., Tromp-van Meerveld, H., Peters, N. E., and Freer, J. E.: Consistency between hydrological models and field observations: linking processes at the hillslope scale to hydrological responses at the watershed scale, Hydrol. Process., 23, 311–319, 2009. 4467

Doody, D. G., Higgins, A., Matthews, D., Foy, R. H., Pilatova, K., Duffy, O., and Watson, C. J.: Overland flow initiation from a drumlin grassland hillslope, Soil Use Manage., 26, 286–298, 2010. 4467

Dramais, G., LeCoz, J., Camenen, B., and Hauet, A.: Advantages of a mobile LSPIV method for measuring flood discharges and improving stage-discharge curves, J. Hydro-Environ. Res., in press, 2011. 4467

Dunkerley, L. D.: Estimating the mean speed of laminar overland flow using dye injection-uncertainty on rough surfaces, Earth Surf. Proc. Land., 26, 363–374, 2001. 4467

Dunkerley, L. D.: An optical tachometer for short-path measurement of flow speeds in shallow overland flows: improved alternative to dye timing, Earth Surf. Proc. Land., 28, 777–786, 2003. 4467

Esteves, M., Planchon, O., Lapetite, J. M., Silvera, N., and Cadet, P.: The “Emire” large rainfall simulator: design and field testing, Earth Surf. Proc. Land., 25, 681–690, 2000. 4473, 4482

Fujita, I. and Kunita, Y.: Application of aerial LSPIV to the 2002 flood of the Yodo River using a helicopter mounted high density video camera, J. Hydro-Environ. Res., in press, 2011. 4467

Fujita, I., Watanabe, H., and Tsubaki, R.: Development of a non-intrusive and efficient flow monitoring technique: The space-time image velocimetry (STIV), Intl. J. River Basin, 5, 105–114, 2007. 4467

Ghahramani, A., Ishikawa, Y., Gomi, T., Shiraki, K., and Miyata, S.: Effect of ground cover on splash and sheetwash erosion over a steep forested hillslope: A plot-scale study, CATENA, 85, 34–47, 2011. 4466

HESSD

9, 4465–4503, 2012

Gomi, T., Sidle, R. C., Miyata, S., Kosugi, K., and Onda, Y.: Dynamic runoff connectivity of overland flow on steep forested hillslopes: Scale effects and runoff transfer, Water Resour. Res., 44, W08411, doi:10.1029/2007WR005894, 2008a. 4466

Gomi, T., Sidle, R. C., Ueno, M., Miyata, S., and Kosugi, K.: Characteristics of overland flow generation on steep forested hillslopes of central Japan, J. Hydrol., 361, 275–290, 2008b. 4467

Gonzalez, R. C., Woods, R. E., and Eddins, S. L.: Digital Image Processing using MATLAB, Pearson Prentice-Hall, Upper Saddle River, NJ, 2004. 4472

Gunn, R. and Kinzer, G. D.: The terminal velocity of fall for water droplets in stagnant air, J. Meteorol., 6, 243–248, 1949. 4482, 4483

Haralick, R. M., Sternberg, S. R., and Zhuang, X.: Image analysis using mathematical morphology, IEEE T. Pattern. Anal., PAMI-9, 532–550, 1987. 4472

Hauet, A., Muste, M., and Ho, H.-C.: Digital mapping of riverine waterway hydrodynamic and geomorphic features, Earth Surf. Proc. Land., 34, 242–252, 2009. 4467

Hudson, J. A.: The impact of sediment on open channel flow measurement in selected UK experimental basins, Flow Meas. Instrum., 15, 49–58, 2004. 4467

Jodeau, M., Hauet, A., Paquier, A., Le Coz, J., and Dramais, G.: Application and evaluation of LS-PIV technique for the monitoring of river surface velocities in high flow conditions, Flow Meas. Instrum., 19, 117–127, 2008. 4468

Lange, J., Greenbaum, N., Husary, S., Timmer, J., Leibundgut, C., and Schick, A. P.: Tracers for runoff generation studies in a Mediterranean region: comparison of different scales, in: Hydrology of the Mediterranean and Semiarid Regions, edited by: Servat, E., Najem, W., Leduc, C., and Shakeel, A., vol. 278, IAHS, Montpellier, France, 117–123, 2003. 4467

LeCoz, J., Hauet, A., Pierrefeu, G., Dramais, G., and Camenen, B.: Performance of image-based velocimetry (LSPIV) applied to flash-flood discharge measurements in Mediterranean rivers, J. Hydrol., 394, 42–52, 2010. 4468

Lee, M. C., Lai, C. J., Leu, J. M., Plant, W. J., Keller, W. C., and Hayes, K.: Non-contact flood discharge measurements using an X-band pulse radar (I) Theory, Flow Meas. Instrum., 13, 265–270, 2002. 4467

Lhermitte, R. M.: Probing of atmospheric motion by airborne pulse-Doppler radar techniques, J. Appl. Meteorol., 10, 234–246, 1971. 4482, 4483, 4503

Löffler-Mang, M.: An optical disdrometer for measuring size and velocity of hydrometeors, J. Atmos. Ocean. Tech., 17, 130–139, 2000. 4482

HESSD

9, 4465–4503, 2012

Maxey, M. R. and Riley, J. J.: Equation of motion for a small rigid sphere in a nonuniform flow, Phys. Fluids, 26, 883–889, 1983. 4468
McGuire, K. J. and McDonnell, J. J.: Hydrological connectivity of hillslopes and streams: Characteristic time scales and nonlinearities, Water Resour. Res., 46, W10543, doi:10.1029/2010WR009341, 2010. 4466
Mügler, C., Planchon, O., Patin, J., Weill, S., Silvera, N., Richard, P., and Mouche, E.: Comparison of roughness models to simulate overland flow and tracer transport experiments under simulated rainfall at plot scale, J. Hydrol., 402, 25–40, 2011. 4466, 4467
Muste, M., Fujita, I., and Hauet, A.: Large-scale particle image velocimetry for measurements in riverine environments, Water Resour. Res., 44, W00D19, doi:10.1029/2008WR006950, 2008. 4467
Muste, M., Ho, H.-C., and Kim, D.: Considerations on direct stream flow measurements using video imagery: Outlook and research needs, J. Hydro-Environ. Res., 5, 289–300, 2011. 4467
Pérez-Latorre, F. J., deCastro, L., and Delgado, A.: A comparison of two variable intensity rainfall simulators for runoff studies, Soil Till. Res., 107, 11–16, 2010. 4473
Planchon, O., Silvera, N., Gimenez, R., Favis-Mortlock, D., Wainwright, J., Le Bissonnais, Y., and Govers, G.: An automated salt-tracing gauge for flow-velocity measurement, Earth Surf. Proc. Land., 30, 833–844, 2005. 4467
Puleo, J. A., McKenna, T. E., Holland, K. T., and Calantoni, J.: Quantifying riverine surface currents from time sequences of thermal infrared imagery, Water Resour. Res., 48, W01527, doi:10.1029/2011WR010770, 2012. 4467
Riley, S. J. and Hancock, F.: A rainfall simulator for hydrologic and erosion experiments on mines, with an example of its applications at Ranger Uranium Mine, Northern Territory, Australia, The Australiasian Institute of Mining and Metallurgy Proceedings, 1, 3–8, 1997. 4473
Scherrer, S., Naef, F., Faeh, A. O., and Cordery, I.: Formation of runoff at the hillslope scale during intense precipitation, Hydrol. Earth Syst. Sci., 11, 907–922, doi:10.5194/hess-11-907-2007, 2007. 4466
Soo, S. L.: Fluid Dynamics of Multiphase Systems, Blaisdell Publishing Company, Waltham, MA, 1967. 4468
Speed, M., Tetzlaff, D., Soulsby, C., Hrachowitz, M., and Waldron, S.: Isotopic and geochemical tracers reveal similarities in transit times in contrasting mesoscale catchments, Hydrol. Process., 24, 1211–1224, 2010. 4467

HESSD
9, 4465–4503, 2012

Tatard, L., Planchon, O., Wainwright, J., Nord, G., Favis-Mortlock, D., Silvera, N., Ribolzi, O., Esteves, M., and Huang, C. H.: Measurement and modelling of high-resolution flow-velocity data under simulated rainfall on a low-slope sandy soil, J. Hydrol., 348, 1–12, 2008. 4467, 4475

Tauro, F., Aureli, M., Porfiri, M., and Grimaldi, S.: Characterization of buoyant fluorescent particles for field observations of water flows, Sensors, 10, 11512–11529, 2010. 4468, 4471, 4472, 4479

Tauro, F., Grimaldi, S., Petroselli, A., and Porfiri, M.: Fluorescent particle tracers for surface flow measurements: a proof of concept in a natural stream, Water Resour. Res., submitted, 2011a. 4468, 4470

Tauro, F., Pagano, C., Porfiri, M., and Grimaldi, S.: Tracing of shallow water flows through buoyant fluorescent particles, Flow Meas. Instrum., accepted, 2011b. 4468

Ticehurst, J. L., Cresswell, H. P., McKenzie, N. J., and Glover, M. R.: Interpreting soil and topographic properties to conceptualise hillslope hydrology, Geoderma, 137, 279–292, 2007. 4466

Uchida, T. and Asano, Y.: Spatial variability in the flowpath of hillslope runoff and streamflow in a meso-scale catchment, Hydrol. Process., 24, 2277–2286, 2010. 4466

HESSD
9, 4465–4503, 2012

Table 1. Classes of particle diameters used for the experiments.

Class	1	2	3	4	5	6	7	8	9
Diameter (μm)	75–90	106–125	150–180	250–300	355–425	500–600	710–850	850–1000	1000–1180

HESSD
9, 4465–4503, 2012

Table 2. Granulometry of the experimental plot. The soil used for the plot can be classified as sand according to the International Society of Soil Science (ISSS).

Soil type	Clay	Silt	Sand
Portion (%)	11.55	21.76	66.69

HESSD
9, 4465–4503, 2012

Table 3. Velocities obtained through the image analysis procedure, IM Velocity, and visual analysis, VA Velocity. VA velocities are reported for the larger classes of diameters since experiments with smaller particles do not allow for accurate travel time estimations.

Diameter μm	IM Velocity $m\,s^{-1}$	VA Velocity $m\,s^{-1}$
75–90	0.08	n.a.
	0.11	n.a.
150–180	0.11	n.a.
	0.18	n.a.
	0.11	n.a.
	1.47	n.a.
	0.46	n.a.
710–850	0.05	n.a.
1000–1180	0.29	0.33
	0.28	0.31
	0.26	0.34

HESSD
9, 4465–4503, 2012

Table A1. Coefficient of uniformity (CU) for the three rainfall simulator configurations. Entries are average CU values obtained by varying the water pressure from 0.4 to 1.8 bar.

Configuration	C1	C2	C3
CU (%) $3 \times 3\,m^2$	75	82	82
CU (%) $5 \times 5\,m^2$	32	66	61

HESSD
9, 4465–4503, 2012

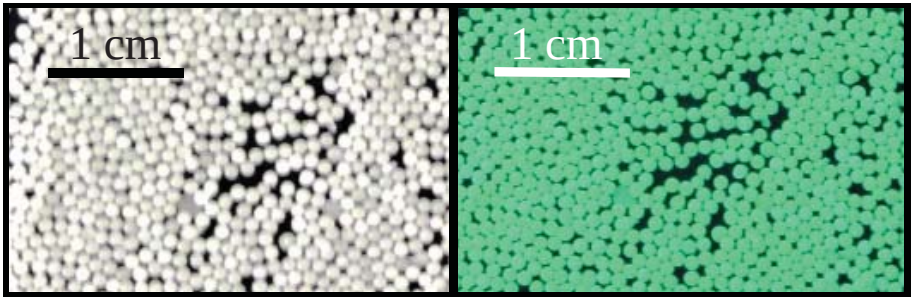

Fig. 1. Left panel: view of a 0.8 mm sample of off-the-shelf fluorescent particles under daylight, and right panel: under 365 nm UV light.

HESSD
9, 4465–4503, 2012

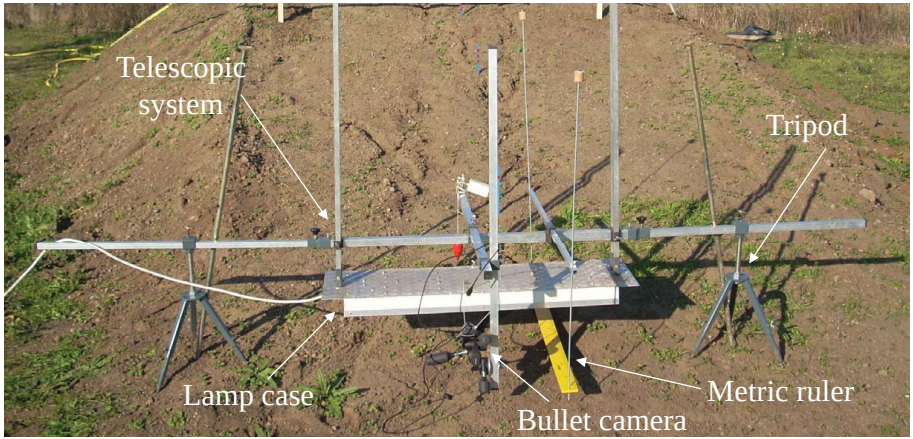

Fig. 2. Experimental apparatus including the light source and the video acquisition units. The metric ruler is used for calibrating acquired videos.

HESSD
9, 4465–4503, 2012

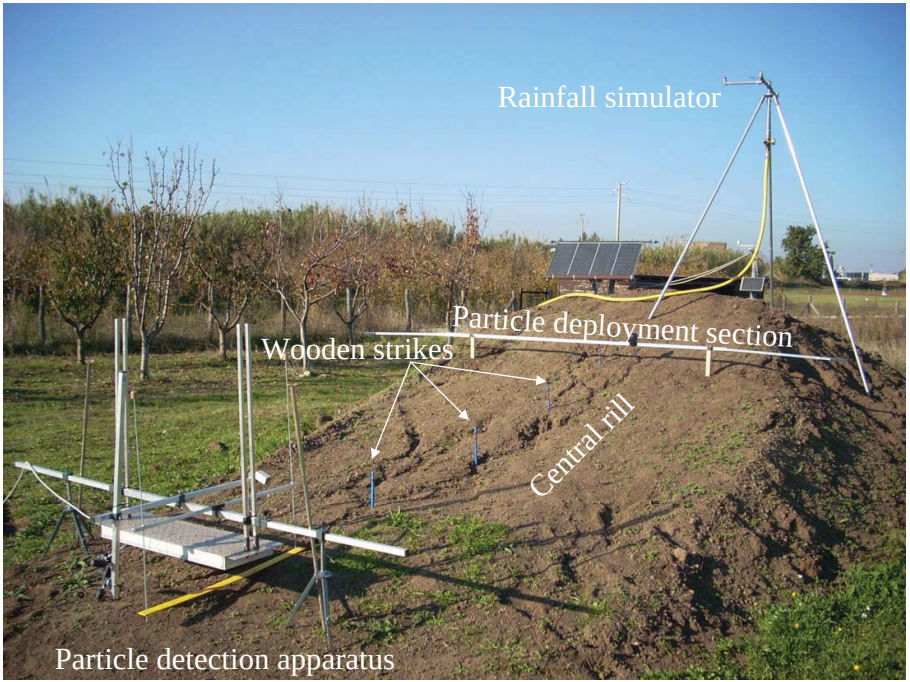

Fig. 3. View of the experimental site depicting the particle detection apparatus and the rainfall simulator.

HESSD
9, 4465–4503, 2012

Fig. 4. View of the rainfall simulator. Water jets are sprayed from two HH22-M 3/8 in and one HH7-M 3/4 in nozzles.

HESSD
9, 4465–4503, 2012

Fig. 5. Beads of smaller diameters trapped at the outside bend of the rill, see red dashed ellipse.

HESSD
9, 4465–4503, 2012

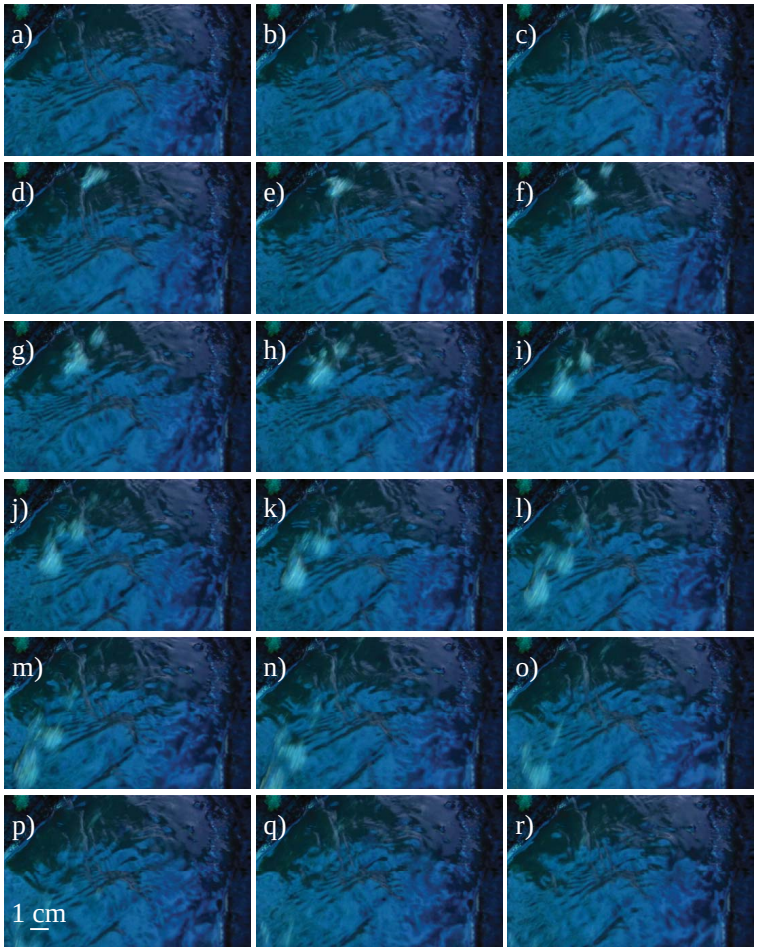

Fig. 6. Sequence of snapshots depicting the transit of a cloud of particles flowing in the rill below the detection apparatus. The diameter of the beads lays in the range 75–90 µm.

HESSD
9, 4465–4503, 2012

Fig. 7. Beads of larger diameters diffuse in the channel due to the presence of sediments and subrills, see red dashed ellipses.

HESSD
9, 4465–4503, 2012

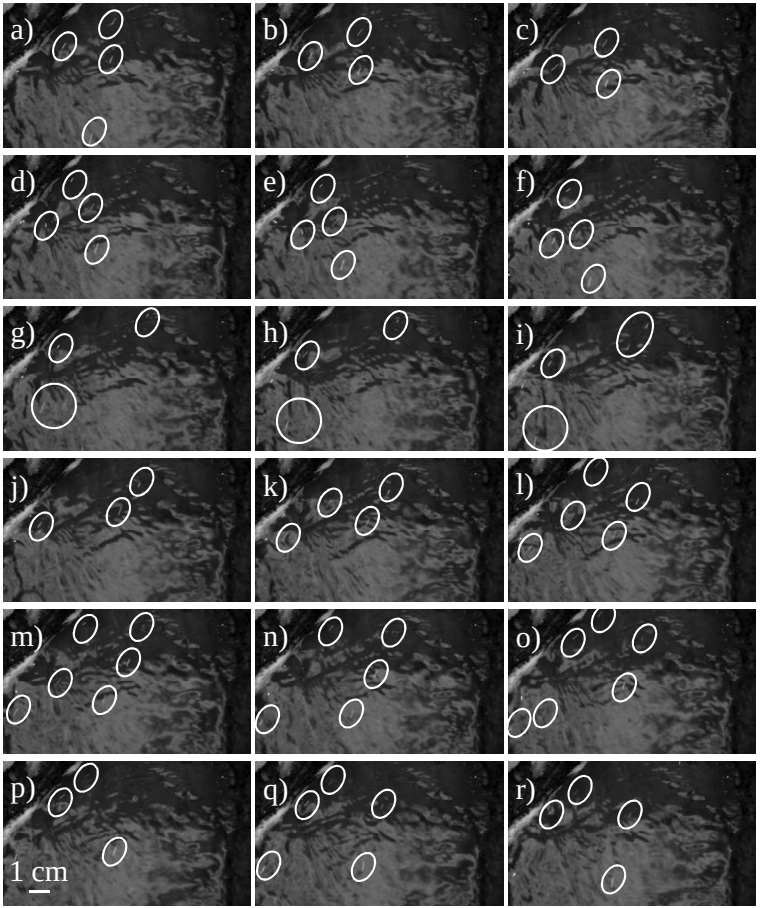

Fig. 8. Sequence of snapshots depicting the transit of single particles flowing in the rill below the detection apparatus. Diameters of the beads are in the range 1000–1180 µm. Only the green channel is reported for clarity.

HESSD
9, 4465–4503, 2012

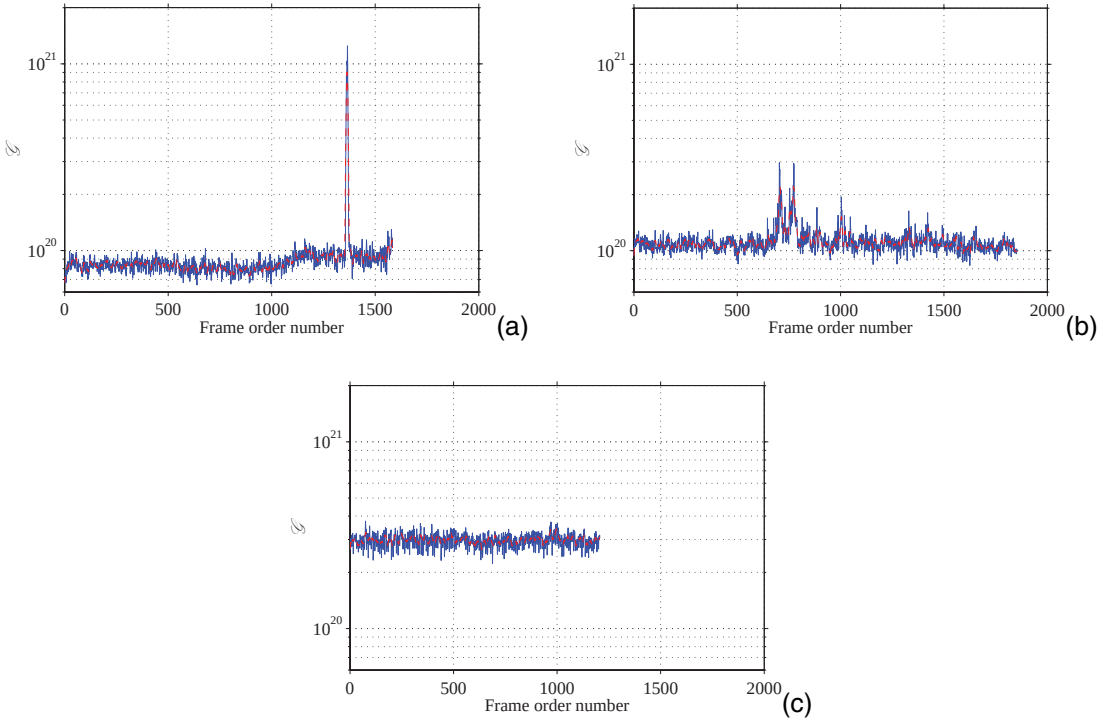

Fig. 9. Index $\mathcal{G}$ for **(a)** beads of 75–90 µm; **(b)** 1000–1180 µm; and **(c)** 500–600 µm. Moving averaged index as obtained from Eq. (1), G, is presented in red.

HESSD
9, 4465–4503, 2012

Fluorescent particle tracers for hillslope observations

F. Tauro et al.

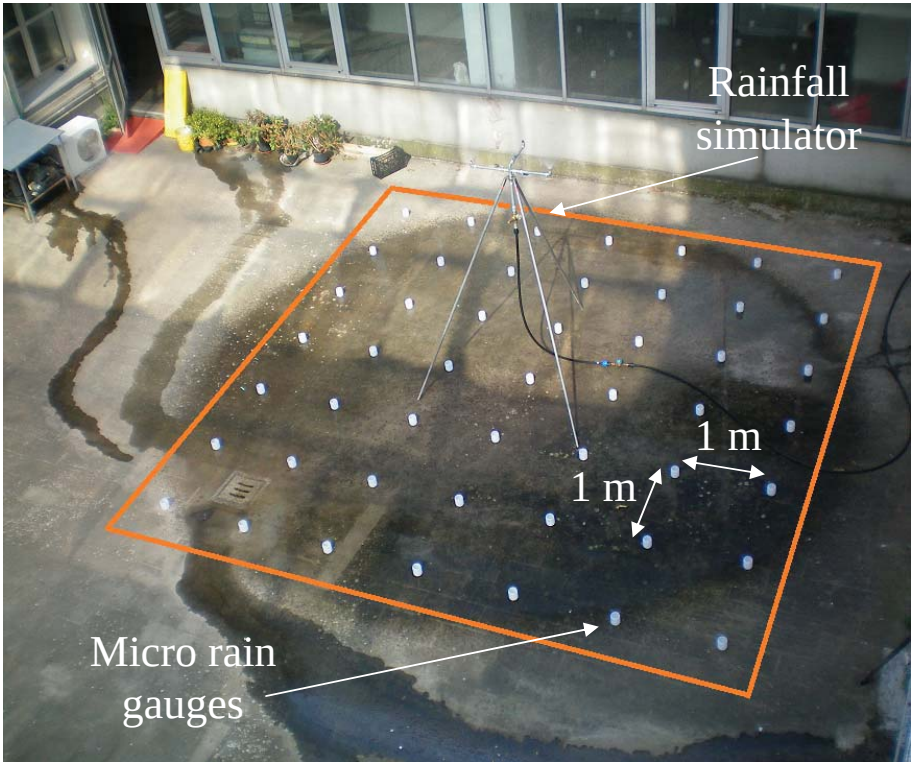

Fig. A1. View of the experimental setup for the rainfall simulator calibration with superimposed micro rain gauges. Micro rain gauges are equally distributed over an area of $7 \times 7\,m^2$.

HESSD
9, 4465–4503, 2012

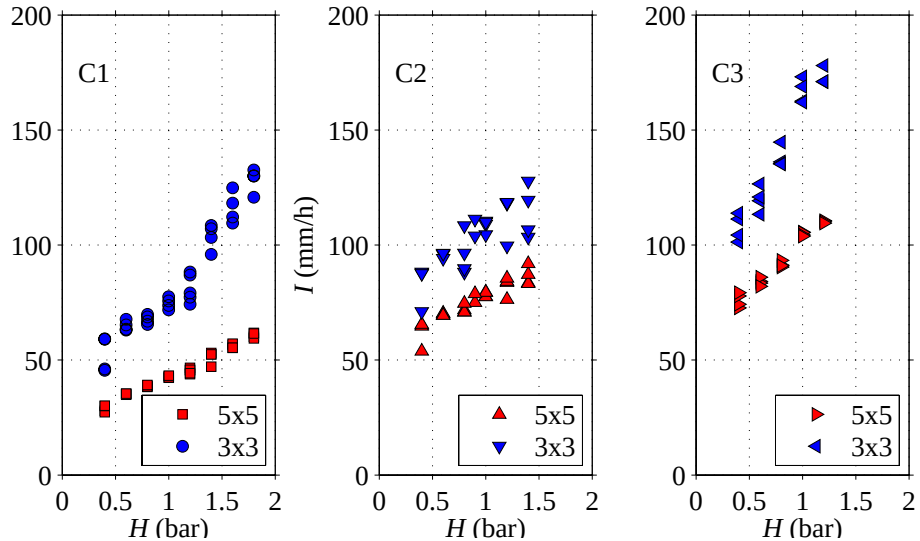

Fig. A2. Left panel: rainfall intensity for C1; center panel, the C2; and right panel: the C3 configurations. Maximum intensities are obtained with the three nozzles spraying simultaneously, that is, for configuration C3.

HESSD
9, 4465–4503, 2012

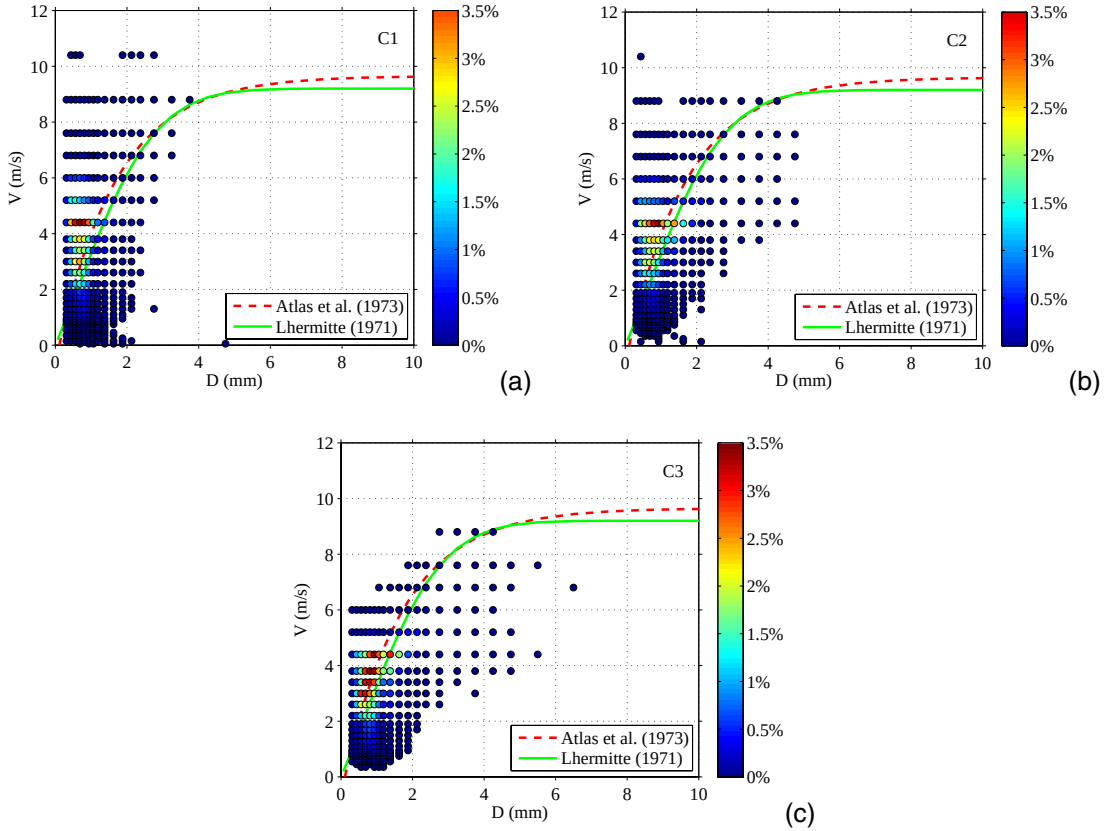

Fig. A3. Drop diameter vs velocity for the **(a)** C1; **(b)** C2; and **(c)** C3 configurations. Colorbar indicates the percentage of hydrometeors for combinations of velocity and diameter. The red dashed curve is obtained through the empirical relation by (Atlas et al., 1973) $V = 9.65 - 10.3\,e^{-0.6D}$, whereas the green solid curve corresponds to the relation developed in (Lhermitte, 1971), $V = 9.2\,[(1 - e^{-(0.11D^2+0.33D)})]$.

HESSD
9, 4465–4503, 2012